Physics of the Solid State, 2025, Vol. 67, No. 12

03,08

Differential tunneling conductance of the n-$Bi_2Te_{3-y}Se_y$ ribbons obtained by melt spinning

© L.N. Lukyanova[1], I.V. Makarenko[1], O.A. Usov[1], S.V. Novikov[1], S.O. Usov[1,2]

[1] Ioffe Institute,
St. Petersburg, Russia
[2] Submicron Heterostructures for Microelectronics, Research & Engineering Center, RAS,
St. Petersburg, Russia
E-mail: lidia.lukyanova@mail.ioffe.ru

Received November 20, 2025
Revised November 20, 2025
Accepted December 15, 2025

The spectra of differential tunneling conductance dI_t/dU versus voltage U, measured by scanning tunneling spectroscopy (STS), were investigated in the ribbons of n-$Bi_2Te_{3-y}Se_y$ ($y = 0.45$) topological insulators formed by melt spinning process and in single-crystal samples with $y = 0.3$. From the analysis of the dI_t/dU spectra, which are proportional to the electronic density of states, the Dirac point energy E_D and its local fluctuations ΔE_D, the positions of the valence E_V and conduction E_C band edges, band gap energy E_g, and the surface concentration of Dirac fermions n_s were determined. It was found that in the n-$Bi_2Te_{2.7}Se_{0.3}$ single crystal, which possess higher Dirac point energy E_D, the fermion surface concentration $n_s = 2.8 \cdot 10^{12}$ cm^{-2} is an order of magnitude higher than in the ribbons. At the same time the power factor in the single crystal is three times higher than in the ribbons. The defect levels associated with donor (Te_{Bi}) and acceptor (Bi_{Te}) antisite defects, as well as tellurium V_{Te} and bismuth V_{Bi} vacancies, were identified within the band gap of the studied thermoelectrics. From the analysis of the STS spectra the additional valence-band subbands VB_i and conduction-band subbands CB_i were revealed.

Keywords: bismuth telluride-based solid solutions, melt spinning, scanning tunneling spectroscopy, topological insulator, Dirac point, defects.

DOI: 10.61011/PSS.2025.12.63079.327-25

1. Introduction

Layered van der Waals solid solutions based on bismuth chalcogenides n-$Bi_2Te_{3-y}Se_y$ are effective low-temperature thermoelectrics for traditional applications as n-branches in thermoelectric generators and refrigerating devices [1,2]. The constant interest in chalcogenide thermoelectrics is related to the fact that they belong to three-dimensional topological insulators (3D-TI) with 2D surface states of Dirac fermions resulting from strong spin-orbit interaction leading to inversion of electronic bands [3–5]. The specific electronic properties of the surface states of Dirac fermions, when the surface acquires metallic properties and the volume is an insulator [3,6], open up new possibilities for using chalcogenide thermoelectrics in various fields of physics: topological electronics [7], photonics [8,9], spintronics [10,11] and for the development of a new class of neuromorphic materials [12].

Despite the insulating properties of volume, there is residual conductivity in 3D materials based on bismuth chalcogenides associated with volumetric defects, some of which can be compensated for by contributions from acceptor and donor intrinsic defects [13,14]; however, this problem has not been completely solved to date.

One of the informative methods for analyzing the topology of thermoelectrics is the method of scanning tunneling spectroscopy (STS), which examines the features of the spectra of differential tunneling conductivity dI_t/dU depending on the applied voltage U, proportional to the electron density of states [15–17]. The Dirac point energy E_D and its fluctuations ΔE_D, the positions of the valence band edge E_V and the conduction band edge E_C, the bandgap width E_g, and the surface concentration of Dirac fermions n_s are determined from the dI_t/dU spectra as a function of U. In addition, from the analysis of the dependences of dI_t/dU on U, information can be obtained on the levels of intrinsic point defects in the band gap of [18] and additional valence and conduction subbands, as shown for solid solutions of p-$(Bi_{1-x}Sb_x)_2Te_3$ [17]. The features of the complex band structure and topological surface states were calculated from the first principles and the strong coupling method in TI of n-type in Bi_2Te_3, Bi_2Se_3 and Bi_2Te_2Se [19].

This paper presents the results of studies of STS spectra in solid solutions n-$Bi_2Te_{2.55}Se_{0.45}$ formed in the form of ribbons by the melt spinning method, in which the melt is rapidly quenched on a rotating a metal refrigerator drum [20,21]. A sample n-$Bi_2Te_{2.7}Se_{0.3}$ obtained by mechanical stratification of a monocrystalline grain cut from an ingot grown by vertical zone alignment was studied for comparison with the ribbons.

2. Differential tunneling conductivity spectra

The characteristics of the differential tunneling conductance spectra dI_t/dU as a function of voltage U were studied by scanning tunneling spectroscopy (STS) on ribbons of solid solutions n-$Bi_2Te_{2.55}Se_{0.45}$ at different speeds of rotation of the drum during melt spinning. The thermoelectrics under consideration have a tetradimite structure and consist of five-layer packages $(-Te(1)-Bi-Te(2)-Bi-Te(1)-)$ for the base material Bi_2Te_3, and are separated by van der Waals slits along interlayer planes (0001) perpendicular to the third-order crystallographic axis c_3. Se atoms replace Te in solid solutions n-$Bi_2Te_{3-y}Se_y$ in five-layer packages.

The ribbons retain the layered structure characteristic of chalcogenide compounds. For the convenience of comparing the results obtained, the measurement samples had fairly close values of the Seebeck coefficient S at room temperature, which in the ribbons n are $Bi_2Te_{2.55}Se_{0.45}$ are $S = -160\,\mu V \cdot K^{-1}$, and in the single crystal sample of n-$Bi_2Te_{2.7}Se_{0.3}$ $S = -170\,\mu V \cdot K^{-1}$.

The STS studies were performed with feedback enabled, with a frequency of 7 kHz and a modulation voltage of 5−10 mV at a fixed height of the tungsten probe above the surface and a resolution of 1.5 mV at room temperature.

During the measurements, it was found that the surface of the ribbons after spinning of the solid solution n-$Bi_2Te_{2.55}Se_{0.45}$ was coated with a thin layer of tellurium oxide with a thickness of about 100 Å with the ribbon thickness of 20 μm. Tunnel contact with the ribbon surface was obtained by lowering the probe through a loose oxide layer to a clean surface to measure the spectra of dI_t/dU depending on the voltage U. dI_t/dU spectra were measured on ribbons with surface treated by Ar^+ ion bombardment and without additional ribbon treatment.

dI_t/dU spectra for fragments of n-$Bi_2Te_{2.55}Se_{0.45}$ ribbons without surface treatment with Ar^+ ions at spinning drum rotation speed $v1$ had flat areas with weakly pronounced minima of dependencies dI_t/dU in a wide range of changes of voltage U from −200 to 200 mV. This character of dependences dI_t/dU on U can be explained by the influence of residual oxide fragments, which prevent the appearance of tunneling current at lower voltages.

It should be noted that the minimum value of dI_t/dU on U in n-type conductivity materials based on Bi_2Te_3 corresponds to the position of the Dirac point E_D, which is located in the band gap [22].

The position of the ceiling of the valence band E_V and the bottom of the conduction band E_C on the dependences dI_t/dU on U relative to the Fermi level $E_F = 0$ is determined by the method of normalized differential conductivity at the inflection points of the curve $(dI_t/dU)/(|I_t|(U))$ [22] or by calculating the second derivative d^2I_t/dU^2 [15].

Parameter data for all measured spectra (Figures 1−4) allowed determining local fluctuations ΔE_D, ΔE_V, ΔE_C and ΔE_g relative to the average values. In ribbons without surface treatment by Ar^+ ions, the energy of the Dirac point E_D and its average value $\langle E_D\rangle = -92$ meV were higher at the spinning speed of $v1 = 26$ m/s (table and Figure 1), and the fluctuations of ΔE_D varied from 5 to 25 %.

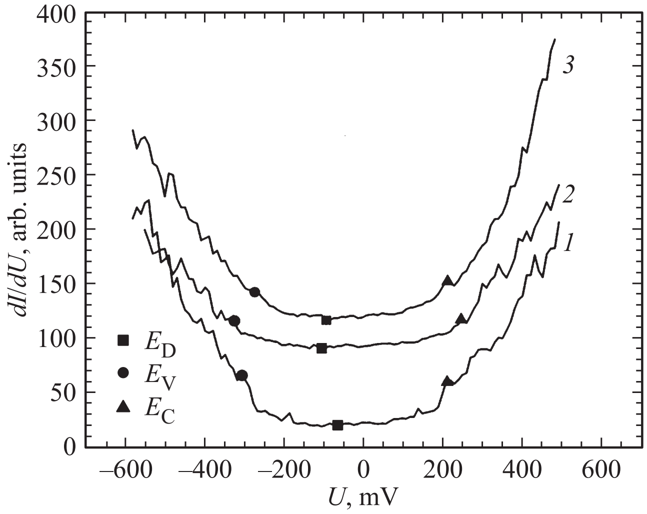

Figure 1. Differential tunneling conductance spectra dI_t/dU depending on voltage U for ribbon fragments (curves 1−3) of solid solution n-$Bi_2Te_{2.55}Se_{0.45}$ without surface treatment with Ar^+ at the spinning drum rotation speed of $v1 = 26$ m/s. E_D is the position of the Dirac point, E_V and E_C is the position of the ceiling of the valence band and the bottom of the conduction band.

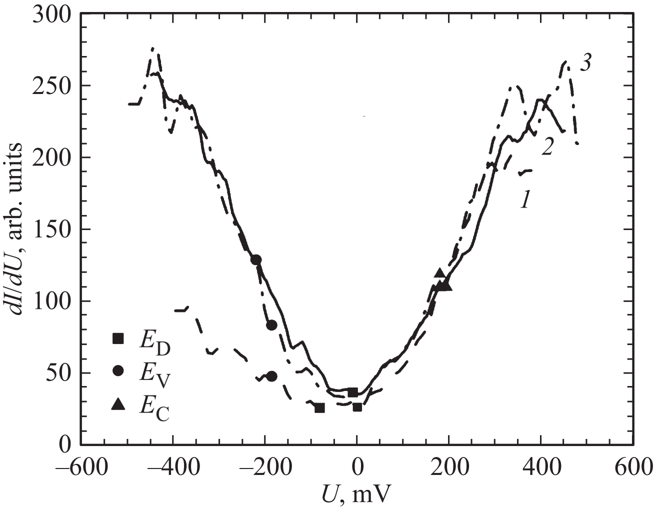

Figure 2. Differential tunneling conductance spectra dI_t/dU depending on voltage U for ribbon fragments (curves 1−3) of solid solution of n-$Bi_2Te_{2.55}Se_{0.45}$ without additional surface treatment at speed of $v2 = 52$ m/s. Notations of E_D, E_V and E_C as in Figure 1.

Fluctuations of ΔE_D significantly increased from 70 to 150 % as the speed increased to $v2 = 52$ m/s at $\langle E_D\rangle = -31.5$ meV (Table and Figure 2). The surface treatment of the ribbons by Ar^+ ion bombardment resulted in a decrease in energies E_D and fluctuations of ΔE_D to 20−30 % for both $v1$ and $v2$ (Table and Figures 3 and 4).

Fluctuations in the ceiling of the valence band ΔE_V and the bottom of the conduction band ΔE_C were insignificant

Parameters of ribbons of solid solutions of n-$Bi_2Te_{2.55}Se_{0.45}$

№. of figures and curves	v, m/s	Treatment of surface	E_D, meV	E_V, meV	E_C, meV	E_g, mV	n_s 10^{11} cm^{-2}
1, *1*	26	–	−69	−311	203	514	5
1, *2*	26	–	−109	−328	240	568	13
1,*3*	26	–	−97	−276	206	482	10.3
2, *1*	52	–	−82	−186	192	378	7.3
2, *2*	52	–	−10.5	−220	178	398	0.12
2, *3*	52	–	−2	−186	178	364	$4 \cdot 10^{-3}$
3, *1*	26	Ar^+	−16	−180	224	404	0.3
3, *2*	26	Ar^+	−18	−162	206	368	0.35
3, *3*	26	Ar^+	−27.5	−191	157	348	0.83
4, *1*	52	Ar^+	−37.5	−225	247	472	1.5
4, *2*	52	Ar^+	−50	−262	187	449	2.7
4, *3*	52	Ar^+	−29.5	−303	182	485	0.95
4, *4**	–	–	−119	−222	15	237	28

Note. * data for a single crystal sample of n-$Bi_2Te_{2.7}Se_{0.3}$.

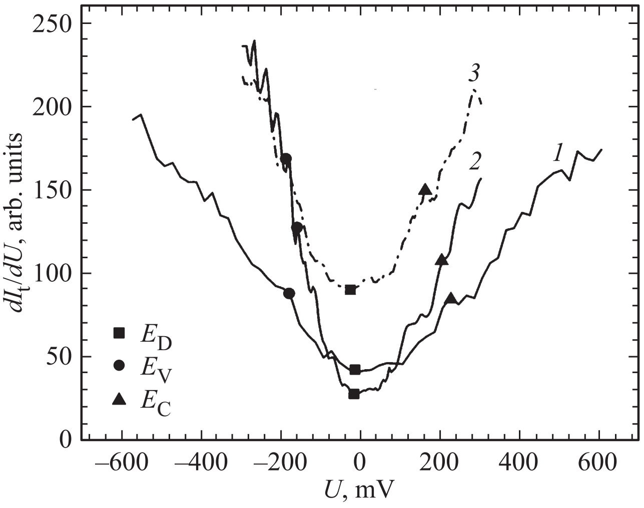

Figure 3. Differential tunneling conductance spectra dI_t/dU depending on voltage U for ribbon fragments (curves *1–3*) of solid solution n-$Bi_2Te_{2.55}Se_{0.45}$obtained by spinning with surface treatment with Ar ions$^+$ at a speed of $v1 = 26$ m/s. Notations of E_D, E_V and E_C as in Figure 1.

and did not exceed 10% regardless of the surface treatment for the speed $v1$. With an increase in the spinning speed to $v2$ in ribbons with a surface treated by Ar^+, fluctuations of ΔE_V and ΔE_C increased on individual surface fragments to 15–20%.

The spectra of dI_t/dU from U in a single crystal sample of similar composition n-$Bi_2Te_{2.7}Se_{0.3}$ were studied for comparison with the ribbons (Table and Figure 4, curve *4*). The energy of the Dirac point E_D in a single crystal n-$Bi_2Te_{2.7}Se_{0.3}$ increased to −120 meV, and fluctuations of ΔE_D decreased [23], which is determined by the higher density of states on the interlayer surface (0001) compared to ribbons.

The band gap width E_g increased with increase of speed from $v1$ to $v2$ during treatment of the surface of the ribbons with Ar^+ ions (Table and Figures 3 and 4). The increase

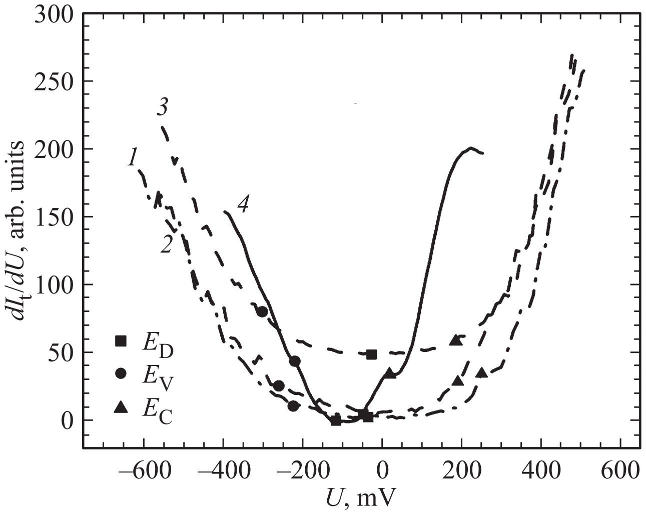

Figure 4. Differential tunneling conductance spectra dI_t/dU depending on voltage U for ribbon fragments (curves *1–3*) of solid solution of n-$Bi_2Te_{2.55}Se_{0.45}$ obtained by spinning with surface treatment with Ar^+ ions at a speed of $v2 = 52$ m/s and (curve *4*) of a single crystal sample of n-$Bi_2Te_{2.7}Se_{0.3}$. Notations of E_D, E_V and E_C as in Figure 1.

of E_g in ribbons without surface treatment with Ar^+ at $\upsilon1$ compared with $\upsilon2$ is associated with flat spectra of dI_t/dU in a wide voltage range from -200 to 200 mV (Table and Figures 1 and 2). Such an increase of E_g on the untreated surface of the ribbons can be explained by the weakly expressed minima of the dependencies dI_t/dU on U in Figure 1.

In the sample of a single crystal n-$\mathrm{Bi_2Te_{2.7}Se_{0.3}}$, the value of E_g was significantly lower (see table). An increase of E_g in the ribbons provides a shift in the onset of intrinsic conductivity to higher temperatures compared to single crystals. Unlike single crystals, the obtained features of the E_D, E_V, E_C and E_g changes in the ribbons are associated with an inhomogeneous distribution of the density of states [24] and with an amplification the effects of structural defects when changing the technological parameters of spinning.

3. Surface concentration of Dirac fermions

The surface concentration of n_s in TI based on $\mathrm{Bi_2Te_3}$ is defined as $n_s = k_\mathrm{F}^2/4\pi$, where the wave vector is $k_\mathrm{F} = |E_\mathrm{D}|/\upsilon_\mathrm{F}$, υ_F is the Fermi velocity [25]. The Fermi velocity υ_F in ribbons of solid solutions n-$\mathrm{Bi_2Te_{2.55}Se_{0.45}}$ was determined by Vegard's law using data for the solid solution system $\mathrm{B_2Te_{3-y}Se_y}$ in accordance with Ref. [26], since for n-$\mathrm{Bi_2Te_3}$ and solid solutions n-$\mathrm{B_2Te_{3-y}Se_y}$ at the specified values of $y = 0$ [26], 0.9 [27], 1 [28] the dependence of the Fermi velocity υ_F on the content of Se atoms in solid solutions is linear, while for ribbons of n-$\mathrm{Bi_2Te_{2.55}Se_{0.45}}$ $\upsilon_\mathrm{F} = 4.1 \cdot 10^5$ m/s, and in sample of n-$\mathrm{Bi_2Te_{2.7}Se_{0.3}}$ $\upsilon_\mathrm{F} = 3.97 \cdot 10^5$ m/s.

The surface treatment of the ribbons of n-$\mathrm{Bi_2Te_{2.55}Se_{0.45}}$ with Ar^+ ions leads to an increase in the concentration of n_s (table and Figure 3, curves *1–3*, Figure 4, curves *1–3*) to maximum values of $2.7 \cdot 10^{11}\,\mathrm{cm^{-2}}$ at $\upsilon2$ (Figure 4, curve *2*), which indicates an increase in the influence of the surface states of Dirac fermions in ribbons with a treated surface. Estimates of n_s showed that significant changes in the value of n_s are observed on various fragments of ribbons for a surface untreated by Ar^+ characterized by an inhomogeneous distribution of the density of states (Table and Figure 1, curves *1–3*, Figure 2, curves *1–3*).

In the sample of n-$\mathrm{Bi_2Te_{2.7}Se_{0.3}}$, the surface concentration was higher by an order of magnitude ($n_s = 2.8 \cdot 10^{12}\,\mathrm{cm^{-2}}$) compared with the ribbons (Figure 4, curve *4*), and therefore the contribution of the surface states of Dirac fermions to the transport properties in single crystals increases. The increase in the contribution of surface states is confirmed by the high power parameter $S^2\sigma$ at room temperature, equal to $44 \cdot 10^{-6}\,\mathrm{W \cdot cm^{-1}K^{-2}}$, where σ is the specific electrical conductivity, whereas in pressed ribbons obtained at spinning speed $\upsilon1 = 26$ m/s, the power parameter was significantly lower and amounted to: $S^2\sigma = 14 \cdot 10^{-6}\,\mathrm{W \cdot cm^{-1}K^{-2}}$ [29].

4. Levels of surface defects

From the analysis of the derivative of the differential tunneling conductance d^2I_t/dU^2, depending on U, peaks with energies of E_p were detected in the band gap, corresponding to surface levels formed by defects (Figure 5) occurring during the formation of ribbons of solid solutions n-$\mathrm{Bi_2Te_{2.55}Se_{0.45}}$ and single crystal n-$\mathrm{Bi_2Te_{2.7}Se_{0.3}}$. These defects create localized electronic states in the band gap with energies that are determined relative to the Dirac point E_D in the form of $E_p(E_\mathrm{D}) = E_p - E_\mathrm{D}$ and can be either positive or negative.

The most common defects in the materials under consideration are donor anti-structural defects of tellurium at bismuth sites $\mathrm{Te_{Bi}}$ and acceptor defects of bismuth at tellurium sites $\mathrm{Bi_{Te}}$ [18,30]. Vacancies of tellurium $\mathrm{V_{Te}}$ and bismuth $\mathrm{V_{Bi}}$ are also possible [18].

The curves *2* and *3* in Figure 5, *a* and *1–3* in Figure 5, *b* were located very close to each other to a friend, and for greater clarity, these curves were shifted along the vertical axis by an arbitrary number. In ribbons with surface treatment by argon ions Ar^+ at $\upsilon1$, the energy ranges of defect levels E_p, determined relative to the Dirac point E_D, were $(-25)-(-180)$ meV for acceptor defects and $(15-220)$ meV for donor defects, Figure 5, *a*, curves *1–3*. With an increase of speed to $\upsilon2$, the intervals of energy E_p were $(-20)-(-230)$ meV for acceptor defects and $(10-180)$ meV for donor defects, Figure 5, *b*, curves *1–3*. When determining the intervals of energy E_p, the maximum and minimum values of E_p were selected for three fragments on the surface of the ribbons.

According to Ref. [18,30], donor defects can be identified as $\mathrm{Te_{Bi}}$ anti-structural defects, and $\mathrm{Bi_{Te}}$ defects can be identified as acceptor defects. Since the values of energy E_p significantly differ in the obtained ranges, in addition to antistructural defects with low energy of formation, the vacancies of tellurium $\mathrm{V_{Te}}$ and bismuth $\mathrm{V_{Bi}}$ can be formed [18], the formation energy of which is several times greater than formation energy of anti-structural defects [31]. As follows from Figure 5, the density of defect levels in the ribbons (Figure 5, *a*) is higher than in a single crystal (Figure 5, *b*), which contributes to more intense phonon scattering and is one of the reasons for the decrease in lattice thermal conductivity in thermoelectrics obtained by spinning the melt [21].

In addition to the levels of intrinsic defects, additional valence subbands VB_i at energies below -390 meV, and conduction subbands CB_i were detected in the spectra d^2I_t/dU^2 (Figure 5 and 6) at energies above 325 meV, the nature of the features of which is qualitatively consistent [17,19]. The schematic diagram of the bands for a ribbon with surface treatment by argon ions Ar^+ obtained at $\upsilon2$ (Figure 6, *b*) is typical for all the studied ribbons (Figure 3 and 4). The Dirac point E_D in the ribbon (Figure 6, *a* and *b*) is located below the Fermi level E_F, which indicates the n-type of conductivity on the surface of the ribbon.

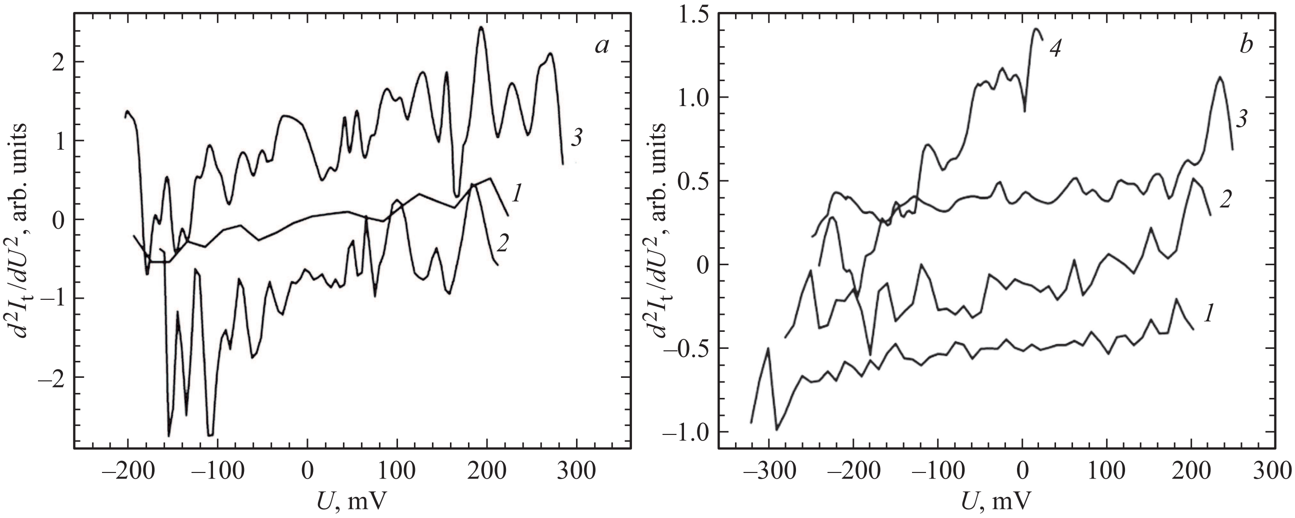

Figure 5. Derivatives of differential tunneling conductance d^2I_t/dU^2 depending on voltage U in ribbons n-Bi$_2$Te$_{2.55}$Se$_{0.45}$ with surface treatment by argon ions Ar$^+$. *a*) $v1 = 26$ m/s (curves *1–3*), it b) $v2 = 52$ m/s (curves *1–3*) for ribbons and dependencies for a single crystal n-Bi$_2$Te$_{2.7}$Se$_{0.3}$ (curve *4*). E_D is the position of the Dirac point. The peaks on the curves*1–3* correspond to the defect levels in the band gap.

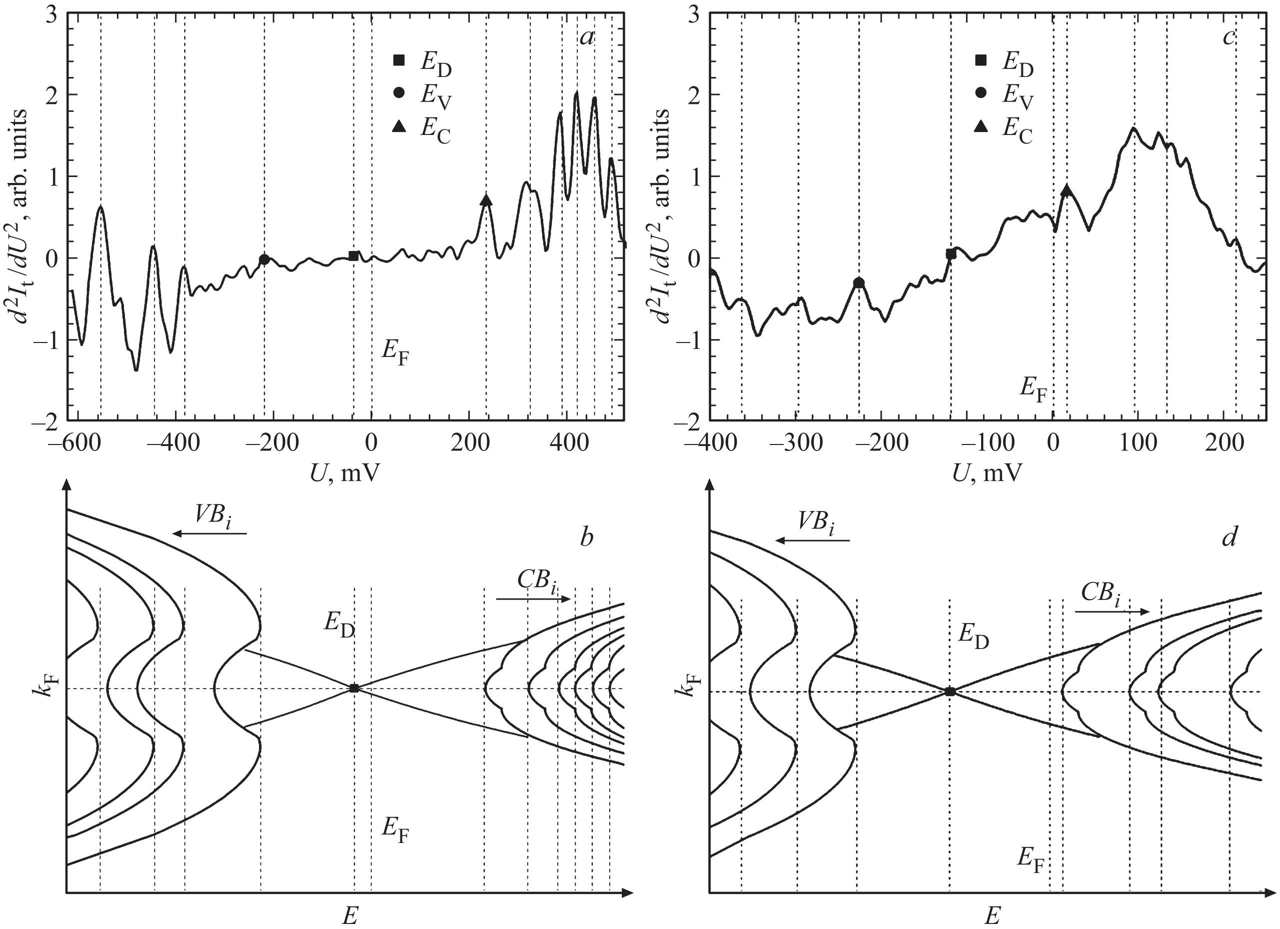

Figure 6. Derivatives of differential tunneling conductance d^2I_t/dU^2 depending on voltage U: *a*) in ribbons of n-Bi$_2$Te$_{2.55}$Se$_{0.45}$ with surface treatment by argon ions Ar$^+$ at $v2 = 52$ m/s and *c*) at n-Bi$_2$Te$_{2.7}$Se$_{0.3}$. E_D, E_V, E_C and E_F — the position of the Dirac point, the ceiling of the valence band, the bottom of the conduction band and the Fermi level, respectively. *b*) Schematic band diagram (*b, d*). The position of the edges of additional valence bands VB$_i$ ($i = 1-4$) and conduction bands CB$_i$ ($i = 1-6$), *d*) VB$_i$ ($i = 1-3$) and CB$_i$ ($i = 1-4$), E — energy, k_F — wave vector.

In a single crystal with a higher Dirac point energy than in ribbons, the point E_D is located significantly below the Fermi level E_F and is shifted towards the valence ribbon. This position E_D in a single crystal is explained by a higher surface concentration of fermions ($n_s = 2.8 \cdot 10^{12}\,\text{cm}^{-2}$), which is significantly higher than in the ribbon ($n_s = 1.5 \cdot 10^{11}\,\text{cm}^{-2}$), see table.

5. Conclusion

The study of the spectra of differential tunneling conductance dI_t/dU in ribbons obtained by spinning a solid solution n-$\text{Bi}_2\text{Te}_{2.55}\text{Se}_{0.45}$ has shown that when the surface of the ribbons is treated with Ar^+ ions the Dirac point energy E_D and its fluctuations were lower than in ribbons with an untreated surface, regardless of the spinning speed from $v1$ to $v2$. At the same time, as the spinning speed increases, the surface concentration of n_s fermions increases.

In ribbons with a surface treated with Ar^+ ions obtained at a speed of $v2$, the surface concentration of Dirac fermions n_s increases to maximum values of $2.7 \cdot 10^{11}\,\text{cm}^{-2}$. However, in a single crystal of n-$\text{Bi}_2\text{Te}_{2.7}\text{Se}_{0.3}$ at a higher Dirac point energy E_D, the value of $n_s = 2.8 \cdot 10^{12}\,\text{cm}^{-2}$ and becomes an order of magnitude higher in comparison with ribbons, which determines the increased influence of the surface states of Dirac fermions on transport properties. At the same time, the power parameter in a single crystal ($S^2\sigma = 44 \cdot 10^{-6}\,\text{W} \cdot \text{cm}^{-1}\text{K}^{-2}$) is three times higher than in ribbons.

The spectra of d^2I_t/dU^2 contained levels of defects in the band gap, which are identified as donor (Te_Bi), acceptor (Bi_Te) antistructural defects, tellurium vacancies V_Te and bismuth vacancies V_Bi.

Additional valence subbands VB_i and conduction subbands CB_i were found on the dependences d^2I_t/dU^2 on U. It follows from the schematic band diagram that the Dirac point E_D in the ribbon, as in a single crystal, is below the Fermi level E_F, which indicates the n-type of conductivity on the surface. At high energy E_D in a single crystal, the Dirac point is shifted towards the valence band, whereas in a ribbon with lower energy E_D it is located near the Fermi level E_F. The position of the Dirac point E_D in a single crystal is explained by the high surface concentration of Dirac fermions compared to ribbons.

Conflict of interest

The authors declare no conflict of interest.

References

[1] D.M. Rowe. Thermoelectric harvesting of low-temperature heat. In: Modules, Systems, and Applications in Thermoelectrics / Ed. D.M. Rowe. CRC Press, Boca Raton (2012).

[2] Thermoelectrics for Power Generation — A Look at Trends in the Technology / Eds S. Skipidarov, M. Nikitin. ISBN 978-953-51-2846-5. InTech (2016). P. 576.

[3] M.Z. Hasan, C.L. Kane. Rev. Mod. Phys. **82**, *4*, 3045 (2010).

[4] J.P. Heremans, R.J. Cava, N. Samarth. Nature Rev. Mater. **2**, *10*, 17049 (2017).

[5] P. Ngabonziza. Nanotechnol. **33**, *19*, 192001 (2022).

[6] Y.L. Chen, J.G. Analytis, J.-H. Chu, Z.K. Liu, S.-K. Mo, X.L. Qi, H.J. Zhang, D.H. Lu, X. Dai, Z. Fang, S.C. Zhang, I.R. Fisher, Z. Hussain, Z.-X. Shen. Sci. **325**, *5937*, 178 (2009).

[7] M.J. Gilbert. Commun. Phys. **4**, *1*, 70 (2021).

[8] G. Jiang, J. Yi, L. Miao, P. Tang, H. Huang, C. Zhao, S. Wen. Sci. Rep. **8**, *1*, 2355 (2018).

[9] L. Zhang, J. Liu, J. Li, Z. Wang, Y. Wang, Y. Ge, W. Dong, N. Xu, T. He, H. Zhang, W. Zhang. Laser. Photon. Rev. **14**, *4*, 1900409 (2020).

[10] W. Han, Y. Otani, S. Maekawa. npj Quantum Mater. **3**, *1*, 27 (2018).

[11] R. Sun, S. Yang, X. Yang, E. Vetter, D. Sun, N. Li, L. Su, Yan Li, Yang Li, Z. Gong, Z.-k. Xie, K.-y. Hou, Q. Gul, W. He, X.-q. Zhang, Z.-h. Cheng. Nano Lett. **19**, *7*, 4420 (2019).

[12] J. Zhu, T. Zhang, Y. Yang, R. Huang. Appl. Phys. Rev. **7**, *1*, 011312 (2020).

[13] A.A. Taskin, Z. Ren, S. Sasaki, K. Segawa, Y. Ando. Phys. Rev. Lett. **107**, *1*, 016801 (2011).

[14] Y. Ando. J. Phys. Soc. Jpn. **82**, *10*, 102001 (2013).

[15] H. Nam, Y. Xu, I. Miotkowski, J. Tian, Y.P. Chen, C. Liu, M.Z. Hasan, W. Zhu, G.A. Fiete, C.-K. Shih. J. Phys. Chem. Solids **128**, 251 (2019).

[16] H. Beidenkopf, P. Roushan, J. Seo, L. Gorman, I. Drozdov, Y.S. Hor, R.J. Cava, A. Yazdani. Nature Phys. **7**, *12*, 939 (2011).

[17] J. Brede, M. Bagchi, A. Greichgauer, A. Uday, A. Bliesener, G. Lippertz, R. Yazdanpanah, A. Taskin, Y. Ando. Phys. Rev. Mat. **8**, *10*, 104202 (2024).

[18] B. Wiendlocha. J. Electron. Mater. **45**, *7*, 3515 (2016).

[19] K.-H. Jin, H.W. Yeom, S.-H. Jhi. Phys. Rev. B **93**, *7*, 075308 (2016).

[20] S. Wang, W. Xie, H. Li, X. Tang. Intermetallics **19**, *7*, 1024 (2011).

[21] S. Fan, J. Zhao, Q. Yan, J. Ma, H.H. Hng. J. Electron. Mater. **40**, *7*, 1018 (2011).

[22] C. Wagner, R. Franke, T. Fritz. Phys. Rev. B **75**, *23*, 235432 (2007).

[23] L.N. Lukyanova, I.V. Makarenko, O.A. Usov. J. Phys.: Condens. Matter **32**, *46*, 465701 (2020).

[24] W.S. Whitney, V.W. Brar, Y. Ou, Y. Shao, A.R. Davoyan, D.N. Basov, K. He, Q.-K. Xue, H.A. Atwater. Nano Lett. **17**, *1*, 255 (2017).

[25] P. Seifert, C. Kastl, A.W. Holleitner. In: Encyclopedia of Interfacial Chemistry: Surface Science and Electrochemistry, Material Aspects of 3D Topological Insulators / Ed. K. Wandelt. Elsevier (2018). P. 491–499.

[26] H. Liu, S. Liu, Y. Yi, H. He, J. Wang. 2D Mater. **2**, *4*, 045002 (2015).

[27] K. Shrestha, V. Marinova, B. Lorenz, P.C.W. Chu. Phys. Rev. B **90**, *24*, 241111(R) (2014).

[28] Z. Ren, A.A. Taskin, S. Sasaki, K. Segawa, Y. Ando. Phys. Rev. B **82**, *24*, 241306(R) (2010).

[29] S.V. Novikov, A.V. Li, A.A. Shabaldin, V.N. Verbitsky, I.A. Nyapshaev. FTT **67**, *5*, 800 (2025) (in Russian).

[30] T. Zhu, L. Hu, X. Zhao, J. He. Adv. Sci. **3**, *7*, 1600004 (2016).

[31] M.W. Oh, J.H. Son, B.S. Kim, S.D. Park, B.K. Min, H.W. Lee. J. Appl. Phys. **115**, *13*, 133706 (2014).

Translated by A.Akhtyamov